Laser-induced graphene on axially oriented alginate–tannic acid–clay aerogel for energy harvesting and storage applications

Journal of Power Sources 670 (2026) 239495

Contents lists available at ScienceDirect

Journal of Power Sources

journal homepage: www.elsevier.com/locate/jpowsour

Laser-induced graphene on axially oriented alginate–tannic acid–clay aerogel for energy harvesting and storage applications

S. Amenta [a,b,1,*], A. Bisceglie [a,1], R. Speranza [a], S. Martellone [a,c], P. Zaccagnini [a,c], L. Baudino [a], J. Gómez-Monterde [d,e,f], L. Marchese [b], M. Sànchez-Soto [d,e,f], A. Lamberti [a,c,**]

[a] Dipartimento di Scienze Applicate e Tecnologia – Politecnico di Torino, Corso Duca Degli Abruzzi 24, 10129, Torino, Italy
[b] Università Degli Studi Del Piemonte Orientale "Amedeo Avogadro", Viale Teresa Michel 11, 15121, Alessandria, Italy
[c] Centre for Sustainable and Future Technologies – Istituto Italiano di Tecnologia, Via Livorno 60, 10144, Torino, Italy
[d] Eb-POLICOM - e-PLASCOM, Department of Materials Science and Engineering, Universitat Politècnica de Catalunya, Barcelona-Tech, EEBE, Barcelona, 08019, Spain
[e] Centre for Research in Multiscale Science and Engineering of Barcelona, Universitat Politècnica de Catalunya, Barcelona-Tech, EEBE, Barcelona, 08019, Spain
[f] Centre Català Del Plàstic, C/Colom 114, Terrassa, 08222, Spain

HIGHLIGHTS

- Bio-based aerogels retain axial anisotropy after LIG conversion.
- LIG DSSC counter electrodes: 2.2 % η, FF 0.72 (1000 lux, GVL electrolyte).
- LIG counter electrodes match platinum performance in DSSCs with identical geometry.
- Aerogel-derived LIG shows 1.49 mF/cm^2 in symmetric supercapacitors with PYR14TFSI.

GRAPHICAL ABSTRACT

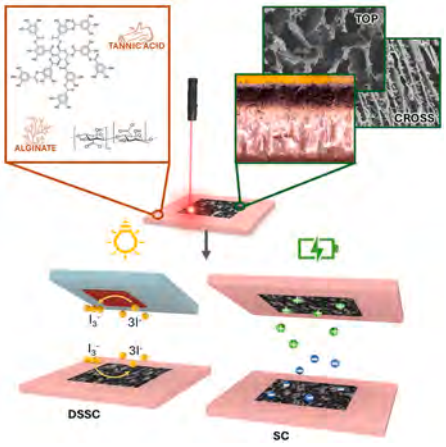

ARTICLE INFO

Keywords:
Laser induced graphene
Anisotropic aerogel
Supercapacitors

ABSTRACT

In this work, a bio-based aerogel with axially oriented morphology was used as a substrate for laser induced graphene (LIG) conversion to fabricate carbon-based electrodes for energy harvesting and storage devices. The substrate materials provide intrinsic flame-retardancy and, together with the anisotropic structure, enable facile and controlled laser writing. The resulting LIG preserves the directional anisotropy of the aerogel, guiding heat propagation. Dye-Sensitized Solar Cells (DSSCs) including the developed material, achieved a fill factor of 0.72

* Corresponding author. Dipartimento di Scienze Applicate e Tecnologia – Politecnico di Torino, Corso Duca Degli Abruzzi 24, 10129, Torino, Italy.
** Corresponding author. Dipartimento di Scienze Applicate e Tecnologia – Politecnico di Torino, Corso Duca Degli Abruzzi 24, 10129, Torino, Italy.
E-mail addresses: serena.amenta@polito.it (S. Amenta), andrea.lamberti@iit.it (A. Lamberti).
[1] These authors contributed equally.

https://doi.org/10.1016/j.jpowsour.2026.239495
Received 20 November 2025; Received in revised form 8 January 2026; Accepted 28 January 2026
Available online 6 February 2026

Dye-sensitized solar cells
Alginate

and photoconversion efficiency of 2.2 % under indoor conditions (1000 lux) using γ-valerolactone (GVL) as the electrolyte solvent. Supercapacitors (SCs) were also developed employing LIG electrodes, exhibiting typical electrical double layer capacitor (EDLC) behaviour and remarkable rate capabilities under both cyclic voltammetry and galvanostatic cycling tests, with negligible resistive losses. The areal capacitance reached 1.49 mF/cm^2, and the Ragone plot showed areal energy and power densities comparable to other sustainable LIG-based SCs. Overall, the aerogel has proven to be a sustainable alternative compatible with laser conversion processes. Remarkably, the aerogel's initial structure is preserved after the laser conversion process, allowing for substrate morphology pre-design to control the final LIG structure. These aerogels' features allow for tailoring carbon-based electrode morphologies toward optimized energy harvesting and storage.

1. Introduction

Since its first isolation in 2004, graphene has captured enduring attention from both academia and industry thanks to its outstanding combination of electrical and thermal conductivity, high current-carrying capacity, mechanical robustness, flexibility, and optical transparency [1]. These unique characteristics have enabled a wide range of emerging applications, including sensors, batteries, supercapacitors, and electrocatalysis [2]. Different methods can be used for graphene production, such as mechanical exfoliation from graphite, chemical vapor deposition, liquid-phase exfoliation, oxidation and reduction processes starting from graphite [3–5]. However, these conventional approaches suffer from several limitations, including low scalability, time-consuming procedures, use of expensive equipment or hazardous chemicals and introduction of structural defects and chemical impurities [1,3–7].

In parallel, extensive research has focused on alternative preparation routes for graphitic and porous carbon materials. Conventional strategies, such as chemical activation and controlled pyrolysis of polymeric precursors, often rely on harsh chemical agents and energy-intensive processing conditions [8,9]. Consequently, increasing attention has been directed toward the development of sustainable carbon synthesis approaches that prioritize scalability, low cost, and environmental compatibility [10,11].

In response to these challenges, laser-induced graphene (LIG) has emerged as a safer and more sustainable alternative [12,13]. The laser-scribing approach offers significant advantages in terms of scalability, cost-effectiveness, and production yield. LIG was discovered by scanning the surface of a polyimide film with a CO_2 laser. When the substrate is irradiated, the laser energy induces a rapid rise in temperature, leading to a photothermal pyrolysis process [14]. Because of the ultrafast temperature rise, the substrate does not have enough time to dissipate heat and stress to its surroundings. As a result, a localized environment with extremely high temperature and pressure is created, which promotes the formation of graphene [15]. This thermal effect helps breaking bonds like C-O, C=O, and N-C, allowing the carbon atoms to reorganize into a sp^2-hybridized lattice [16]. In addition, the gas evolution acts as template during the process, resulting in the formation of porous graphene-like structure [17].

In recent years, significant progress has been made in extending LIG fabrication to various polymeric substrates, many of which share high-thermal stability and flame retardancy [18]. Particularly, increasing attention has been directed towards bio-based and sustainable materials, such as those derived from cellulose or lignin, which not only come from renewable resources but also exhibit high char-forming ability [19,20]. For instance, LIG can be synthesized from paper. However, undesired combustion and ablation must be controlled. To this end, paper and other cellulose-based substrates are often coated with flame-retardant [21] or heat-insulating layers [22]. Beyond sustainability, the intrinsic anisotropy of fibrous bio-based substrates can provide directional heat dissipation and enhanced electrical conductivity, which can be exploited to tailor LIG properties [23].

An emerging bio-based substrate of interest is sodium alginate, a linear polysaccharide polymer derived from brown algae. To date, only a few studies have reported its use for LIG production [24,25]. Alginates inherently exhibit high resistance to flame and do not release harmful gases upon combustion [26]. This property can be further enhanced through the incorporation of tannic acid (TA), a natural polyphenolic compound that also undergoes direct laser writing [27]. Due to its aromatic structure containing sp^2-hybridized carbon atoms, TA can be efficiently converted into LIG [28]. Zhao et al., 2025, successfully employed a composite film of TA and polyvinyl alcohol to fabricate three-dimensional porous graphene using direct laser writing [28].

Aside of precursor selection, electrode architecture has been widely recognized as a critical parameter governing electrochemical performance [29,30], as hierarchical porosity and high surface area are of paramount importance for electrochemical performance. While most LIG studies focus on the optimization of laser parameters for porosity control, only a few have explored laser processing of hierarchical porous substrates. To the best of authors' knowledge, only one paper has demonstrated laser writing on an aerogel precursor. Through laser processing, a resorcinol-formaldehyde aerogel undergoes a transformation into conductive carbon aerogel, retaining its hierarchical porosity [31].

The unique combination of chemical stability, electrical conductivity, and mechanical robustness makes LIG a promising electrode material for energy conversion and storage. One particularly underexplored application is its implementation as a counter electrode (CE) in dye-sensitized solar cells (DSSCs). In these cells, light absorption by a dye injects electrons into a semiconductor (typically TiO_2), which then flow through an external circuit to generate electricity, while an electrolyte with a redox mediator regenerates the dye. LIG offers a sustainable alternative to the conventional platinum CE and redox catalyst, a costly and critical raw material. The high electrical conductivity, large surface area and porous architecture of LIG provide abundant catalytic sites and facilitate electrolyte diffusion, potentially enhancing device efficiency [32].

Similarly, in supercapacitors, LIG is well suited as an electric doble-layer capacitor (EDLC) electrode material. In EDLCs, energy storage occurs through the electrostatic accumulation of ions at the electrode-electrolyte interface, making the performance dependent on the accessible surface area and electrode material electrical conductivity. LIG offers easily tuneable fabrication on various substrates without the use of binders, solvents or other processing steps typically required for current collector-based routes. Such a method can reduce production costs and process limitations associated with electrode integration, enabling the development of scalable and flexible devices [33].

In this work, we demonstrate for the first time the conversion of a fully bio-derived, flame-retardant composite aerogel featuring axially aligned hierarchical pores into LIG. The study elucidates the influence of aerogel architecture on LIG formation and demonstrates its implementation as a multifunctional electrode in both DSSCs and supercapacitors. The results show that LIG can be successfully generated while preserving the intrinsic aerogel porosity, establishing a low-cost and sustainable electrode alternative with strong potential for advanced energy conversion and storage applications.

2. Experimental section

2.1. Materials

Ammonium alginate (AA) (Cecalgum A 500, 350–450 mPa s) with a mannuronic to guluronic acid ratio of 1.37 was purchased from Algaia (Paris, France). Sodium montmorillonite (MMT) clay (PGW grade, $\rho = 2.6$ g/cm^3) from Nanocor (Hoffman Estates, IL, USA). Tannic Acid (TA) in powder form 1701.2 g/mol from Merck (Barcelona, Spain). Fluorine-doped tin oxide (FTO)-coated glass (7 Ω sq^{-1}) and Ruthenizer 535-bisTBA (N719, dye) form Solaronix. Transparent nanoparticle TiO_2 paste from Dyesol (18NR-T). Sodium Iodide, Iodine and γ-valerolactone (GVL) from Sigma-Aldrich while Methoxypropionitrile (MPN) and 4-tert-butylpyridine from Merck. Activated carbon (AC) YP-50F powder from Kuraray. Carbon black (CB) C65 powder from Imerys. Hydroxypropyl cellulose (HPC) Mw 370,000, from Sigma-Aldrich. [PYR14][TFSI] ionic liquid, 99.9 % purity, was purchased by Solvionic. Whatman Glass microfiber grade GF/D (675 μm thickness) from Sigma-Aldich.

2.2. Aerogel preparation

Following the synthesis proposed in Ref. [34] the aerogels were prepared as outlined. The gel precursors were prepared by separately dispersing 5 g of ammonium alginate (AA) and 2 g of MMT clay (C) in 40 mL of DI water, while dissolving 2g tannic acid (TA) powder in 20 mL of DI water. The MMT dispersion was mixed with the TA-alginate blend and homogenized 9000 rpm (IKA T-25 Ultra-Turrax) for 20 min. The mixture was casted onto copper plates with a thickness of ~1 mm and aged for 3 h. To achieve axial orientation, the copper plate supporting the samples was brought into contact with liquid nitrogen (−196 °C) to allow freezing from the bottom upwards, lastly the frozen samples were freeze-dried at −80 °C and 0.02 mbar (Telstar, Terrassa, Barcelona, Spain).

2.3. LIG conversion

A CO_2 laser engraver (Colibrì – Laser Veronese, $\lambda = 10.6$ μm, $P_{max} = 10$ W) was employed to fabricate LIG patterns onto aerogels substrates. Prior to laser processing, aerogels underwent dehydration in a Büchi oven at 60 °C for 5 h to eliminate residual moisture. Laser patterning was conducted under ambient atmospheric conditions, with all sample positioned at the focal plane. Lasing power was varied from 7 to 8 W in 0.5 W increments. Scanning speed was tested at 500, 1200 and 2000 mm/s while pulsed frequency was fixed at 5 Hz.

2.4. Pseudo-reference and counter electrode fabrication

For three electrodes measurements a slurry with the same composition as above (85 wt% AC, 10 wt% CB, 5 wt% HPC) prepared in water (17 wt% solid fraction) was cast onto Al foil by the doctor blade method (150 μm wet thickness). Rectangular electrodes were employed as counter and pseudo-reference in a three-electrode configuration.

2.5. Materials characterization

Cross sections were observed under optical microscopy using a KERN optics OBN 135.

The morphological microstructure of both the pristine aerogel and the inducted LIG were observed using a SUPRA 40 (Zeiss) scanning electron microscope (SEM) operating at 10 kV accelerating voltage and 30 μm aperture. To make samples conductive and mitigate charging effects during imaging, they were sputter-coated with a 20 nm platinum layer using a Q150T ES sample preparation system (Quorum Technologies Ltd). Energy-Dispersive X-ray (EDX) analysis was carried out on LIG samples using a Si(Li) detector (Oxford Instruments) and employing an accelerating voltage of 15 kV and 60 μm aperture.

Fourier transform infrared (FTIR) spectra of pristine aerogel were recorded using a Nicolet 6700 spectrophotometer with a resolution of 1 cm^{-1} (Thermo Fisher Scientific, Waltham, MA, USA) in the attenuated total reflectance mode.

ThermoGravimetric Analysis (TGA) was used to assess thermal stability of the aerogel, using a Mettler Toledo TGA/DSC 1 instrument (Mettler Toledo, Columbus, OH, USA). Approximately 10 mg of the samples were placed in aluminium pans and heated from 30 to 600 °C at a rate of 10 °C/min under a dry nitrogen atmosphere. Thermal transitions of pristine aerogel were analyzed using differential scanning calorimetry (DSC) performed with a Q2000 model (TA Instruments, New Castle, DE, USA). Approximately 5 mg of the samples were encapsulated and subjected to a controlled heating rate of 10 °C/min between 0 and 80 °C. The tests were conducted in an inert nitrogen atmosphere with a gas flow rate of 50 mL/min.

Chemical structure analysis of LIG samples was performed using a Renishaw micro-Raman spectrophotometer with a $\lambda = 514$ nm excitation source. For each sample, triplicate single-point measurements were carried out at randomized locations. Peak deconvolution was carried out by fitting the D, G, and, when applicable, D′ peaks with three Pseudo-Voigt functions. Gaussian functions were used for the D* and D″ peaks, following the commonly adopted method reported in the literature [35–38]. For the second order region [2400–3000] cm^{-1}, three Lorentzian functions were applied, consistent with previous studies [38,39]. I_D/I_G and I_{2D}/I_G ratios were quantified from post-processed spectra.

X-Ray Photoelectron Spectroscopy (XPS) was performed on pristine aerogel sample and LIG samples using a PHI VersaProbe II Hybrid system (Physical Electronics, Inc. (PHI), Chanhassen, MN, USA). Monochromatic Al Kα (1486.6 eV) was used as X-ray source The C–C sp^2 peak in graphitic structures (284.5 eV) was used as reference for calibration. Wide-energy and high-resolution (HR) XPS spectra were collected and processed using CasaXPS software (version 2.3.26) [40]. HR spectra deconvolution into individual mixed Gaussian–Lorentzian and asymmetric peaks was obtained after Shirley background subtraction and binding energy (BE) calibration.

The porosity of both the aerogel and the LIG was calculated using eq. (1). Where ρ_r is the relative density determined by calculating the ratio of the bulk density (ρ_b) to the skeletal density (ρ_s) performed using a helium pycnometer (Micromeritics AccuPyc 1330, Norcross, GA, USA).

$$P = (1 - \rho_r) \cdot 100 \quad (1)$$

Specific Surface Area (SSA) measurements were carried out on both aerogel and LIG in order to examine the impact of laser writing settings on the active material effective SSA. At 77 K, N_2 sorption porosimetry was carried out using ASAP2020 Plus, Micromeritics.

2.6. Devices assembly and characterization

For DSSCs fabrication, FTO-coated conductive glass substrates were cleaned for 30 min in an ultrasonic bath with deionized water and detergent, acetone, and ethanol, then heated at 100 °C for 10 min to ensure complete solvent removal. To prepare the photoanodes, transparent TiO_2 layers were deposited by screen printing (61–64 mesh, two layers), each dried at 100 °C for 10 min. The films were then sintered by heating to 475 °C at 120 °C h^{-1}, holding for 30 min, and cooling to 70 °C, over 5 h. The resulting photoanodes had an active area of 0.36 cm^2 and a thickness of 7–8 μm. After calcination, they were immersed overnight in N719 dye solution (0.3 mM in ethanol). Counter electrodes were prepared as follows: (i) LIG–aerogel (as described above); (ii) Pt-coated FTO, fabricated via sputtering of a thin Pt film from a platinum target with a Q150T ES system (Quorum Technologies Ltd.); (iii) AC slurry cast onto aerogel by the doctor blade method (150 μm wet thickness). The slurry composition was 85 wt% AC, 10 wt% CB, and 5 wt % HPC, with a 17 % solid fraction in ethanol. Cell assembly was performed as follows: for LIG/aerogel and AC/aerogel electrodes, a

titanium grid was placed on top of the active material as current collector, and a glass slide was placed on top of the Ti grid to keep it in place and to allow sealing. The other side of the aerogel layer interfaced with the photoanode and was filled with the electrolyte (Fig. 1a). For Pt-coated FTO electrodes, two configurations were used. In one case the pristine aerogel was positioned between counter electrode and photoanode and filled with the electrolyte (Fig. 1b). In the other case the aerogel was used only as a spacer to maintain the interelectrode distance equal to the previous cases, with the free space between the photoanode and the counter electrode was fully filled by liquid electrolyte (Fig. 1c). Finally, the assembled cells, were locked in place applying pressure, and sealed with UV glue.

For SCs preparation, pouch cells were assembled under argon atmosphere within a glovebox. Each cell employed a glass fiber separator soaked with 300–400 μL of [PYR14][TFSI] as electrolyte. Battery-grade Al foil (15 μm thickness) was used as current collector to probe LIG contacts. For the three-electrode characterization, the laser-processed aerogel was employed as the working electrode, while an activated carbon (AC) electrode served as the quasi-reference electrode [41], and a second AC electrode was used as the counter electrode (Fig. 1d). A sandwich architecture was adopted in order to replicate the conditions of the final stack. For device testing, LIG electrodes were employed in symmetrical EDLC design and assembled in a stacked configuration, as displayed in Fig. 1e.

DSSCs were characterized by means of an Autolab PGSTAT128 potentiostat with a FRA32M module, EIS measurements were carried out in the dark at 0.6 V. EIS measurements were carried out at V_{oc} biases with a signal amplitude of 10 mV in the frequency range of 100 kHz to 100 mHz. The DSSC current density–voltage (J–V) response was recorded using the same device. The scan rate used to record the J-V curves was 20 mV/s. Measurements under AM 1.5 G light spectrum were conducted using a Newport 91195 A solar simulator (using a mask to obtain an area of 0.25 cm^2), while measurements under indoor illumination conditions were conducted using a Delta OhmHD 2102.2 photo/radiometer and a warm white LED lamp (12–60 V AC/DC, 10W, 3000 K, 810 lm from SPL).

All electrochemical measurements for SCs were carried out at room temperature using a BioLogic VMP-3 multichannel potentiostat controlled by EC-Lab software. The produced LIG was characterized in a three-electrode configuration prior to device assembly to perform charge balancing. The LIG electrode was stabilized by symmetric cyclic voltammetry (CV) cycling at ± 0.1 V vs. Open Circuit Potential (OCP) at 5 mV/s for 20 cycles, followed by a stepwise polarization in 0.1 V increments. Independent tests were conducted to determine LIG anodic and cathodic polarization limits. Electrochemical impedance spectroscopy (EIS) was exploited as benchmarking test to ensure that anodic and cathodic experiments were run on equivalent nominal cells. Coulombic efficiency was adopted to determine anodic and cathodic polarization limits. For electrode balancing, the following relationship must be satisfied:

$$Q_+ = Q_- \tag{2}$$

where Q_+ and Q_- are the areal discharge charges of the LIG electrodes under anodic and cathodic polarization, respectively. The ratio between these values defines the electrode area ratio for a balanced device.

Device characterization included EIS, cyclic voltammetry (CV), and galvanostatic charge–discharge (GCD). EIS was conducted with 5 mV

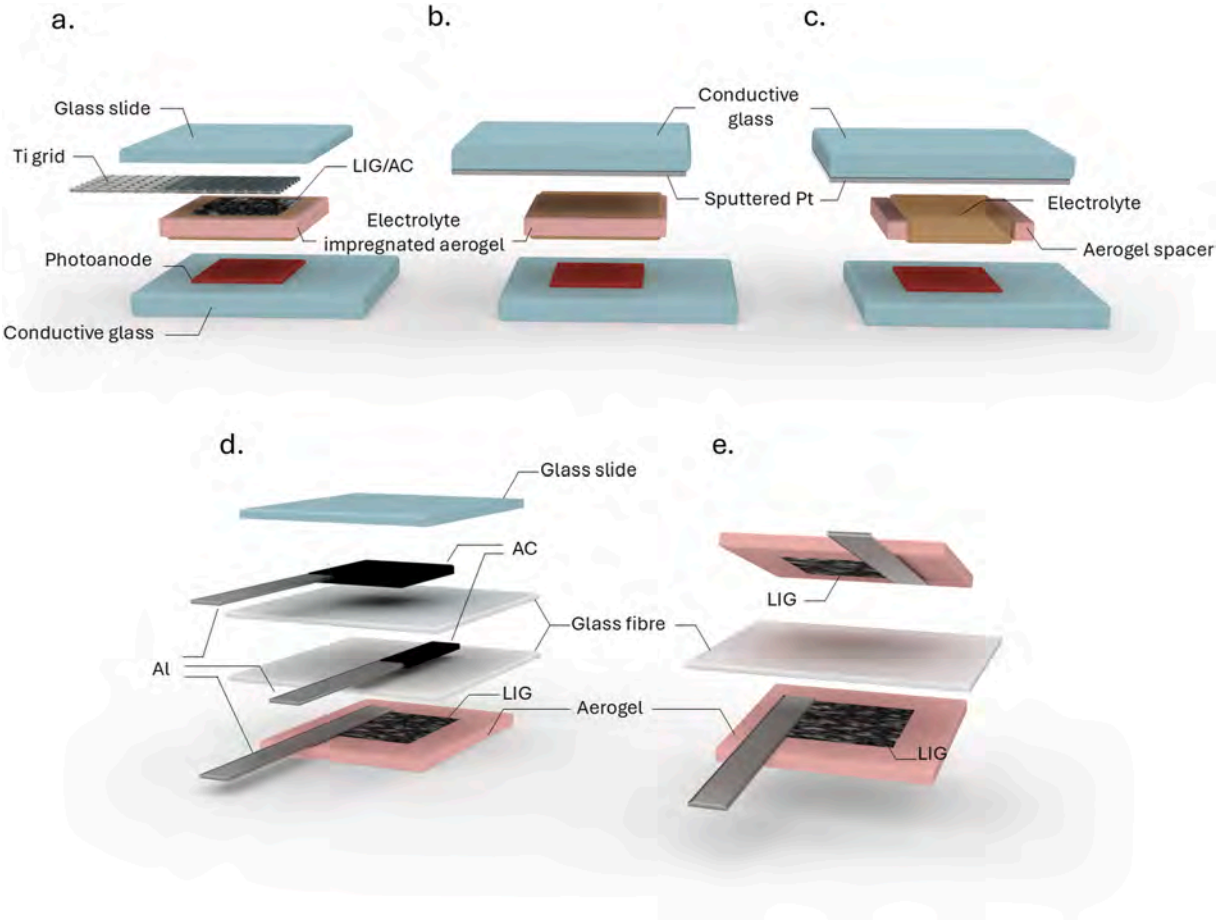

Fig. 1. Configurations used for the DSSCs: (a) AC and LIG CE; (b) Pt CE and aerogel as separator; and (c) Pt CE and liquid electrolyte, maintaining the same interelectrode distance as in the other cases. Setups used for SCs characterization: (d) three-electrodes measurement setup and (e) device assembly.

signal amplitude sweeping frequencies from 1 MHz to 10 mHz, using 10 points per decade and averaging four cycles per frequency. CVs of the assembled device were performed at {5, 10, 20, 50, 100, 200} mV/s. GCD experiments were run at different current densities of {5, 10, 20, 50, 100, 200} μA/cm^2. From the GCD measurements performed on the device, the capacitance values were extracted using the following expressions:

$$C = \frac{1}{2}\frac{Q^2}{E} \tag{3}$$

Where the energy E for the capacitive systems is computed as:

$$E = \int V(t)I(t)\,dt \tag{4}$$

While the charge can be calculated by applying:

$$Q = \int I(t)\,dt \tag{5}$$

The power was derived from the relation:

$$P = \frac{E}{\Delta t} \tag{6}$$

Areal specific quantities were reported by dividing the computed quantities by the LIG electrodes area.

3. Results and discussion

3.1. Aerogel properties

A bio-based aerogel based on AA, TA, and MMT was prepared by freeze-drying and using a bottom-up freezing method to achieve axial alignment of the pores, with a formulation similar to that studied in a previous work, but with a lower clay content [34]. This adjustment was made to retain the structural reinforcement provided by MMT clay while minimizing its proportion, given that the clay acts as a "passive" component that cannot be converted into laser-induced graphene. Scanning electron microscopy (SEM) was performed to evaluate the aerogel structure. Although the reduced clay content, SEM observations show that the overall lamellar architecture and pore orientation are preserved, exhibiting no significant structural changes. The sample retains a well-aligned, honeycomb-like structure along the freezing direction (Fig. 2). Pore dimensions are close to 10 μm, with a porosity of 97.2 ± 0.3 % and a SSA of 1.53 ± 0.03 m^2/g (S.1). These findings show that the freeze-casting method successfully regulates the microstructure, and the aerogel successfully maintains its oriented and interconnected network.

FTIR/ATR analysis (Fig. 3a) enabled the study of the uniformity of the aerogel matrix and the interaction between the different components. The wide peak at 3217 cm^{-1} is related to the –OH stretching and to the asymmetric/symmetric stretching of N–H of the alginate backbone. Peaks at 1089 cm^{-1} and 1030 cm^{-1} are assigned to C–O stretching of ether/ester groups, and C–O–C vibrations of the cyclic ether bridge in the saccharide structure. The latter also overlaps with Si–O–Si vibrations of MMT tetrahedral sheets, confirming the preservation of the clay structure into the composite matrix [42]. The 3610 cm^{-1} band, attributed to Al–OH, Si–OH, and Mg–OH vibrations, appears slightly red-shifted compared with pristine MMT (3616 cm^{-1}), suggesting the formation of hydrogen bonds between the phenolic groups of TA and the –OH/COO$^-$ groups of MMT and alginate. The incorporation of TA is also evidenced by the peaks at 1208 cm^{-1} (C–O stretching of the phenolic groups) and 1714 cm^{-1} (C=O stretching) [43]. The red shift of the phenolic C–O band compared with free phenols (1210–1240 cm^{-1}) confirms hydrogen bonding with alginate carboxylates. Additionally, the 1319 cm^{-1} band, attributed to the C–O–H deformation of phenolic groups in TA, supports these interactions [44–46]. In the low frequency region (<500 cm^{-1}), intense peaks corresponding to Si–O–Si, Al–O–Si, and Al–O–Al bending vibrations are observed, with a distinct Al–O–Si band confirming that the layered MMT structure remains intact within the polymer matrix [47].

Thermogravimetric analysis (TGA) (Fig. 3b) was used to examine the thermal characteristics of the composite aerogels. Physiosorbed water was responsible for the initial 15 % weight reduction in the aerogel. The composite exhibited higher thermal stability compared to pure alginate, as evidenced by a higher onset of decomposition at 5 % mass loss after water evaporation (T_{onset} = 200 °C) and maximum decomposition temperature (T_{dmax} = 226 °C), compared to 189 °C and 224 °C for the

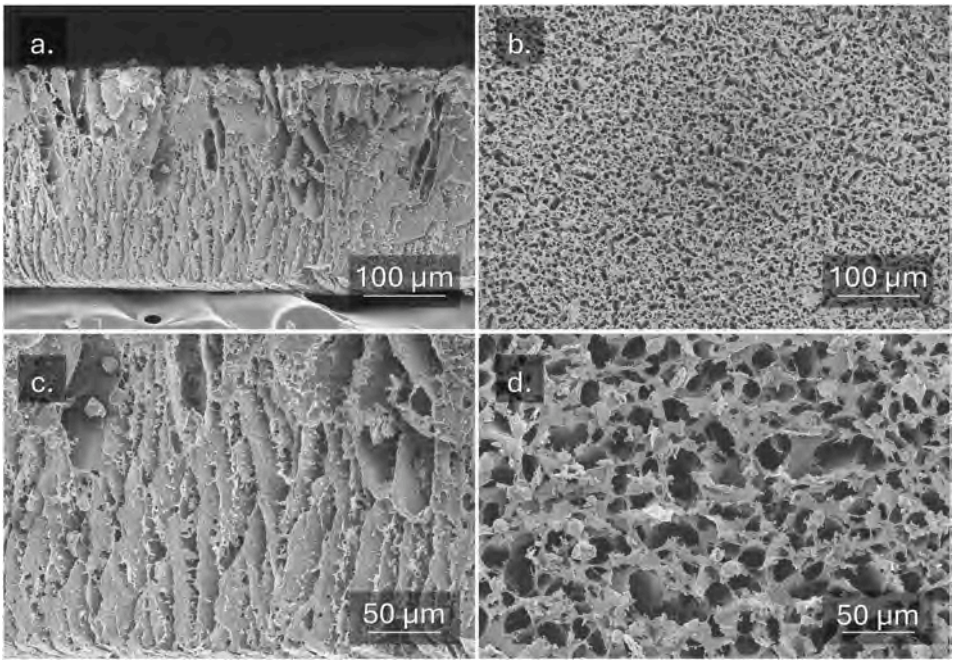

Fig. 2. SEM micrographs of the alginate-MMT clay aerogel composite showing (a. And c.) cross-sectional and (b. And d.) top-view morphologies (scale bars: 100 μm and 50 μm, respectively).

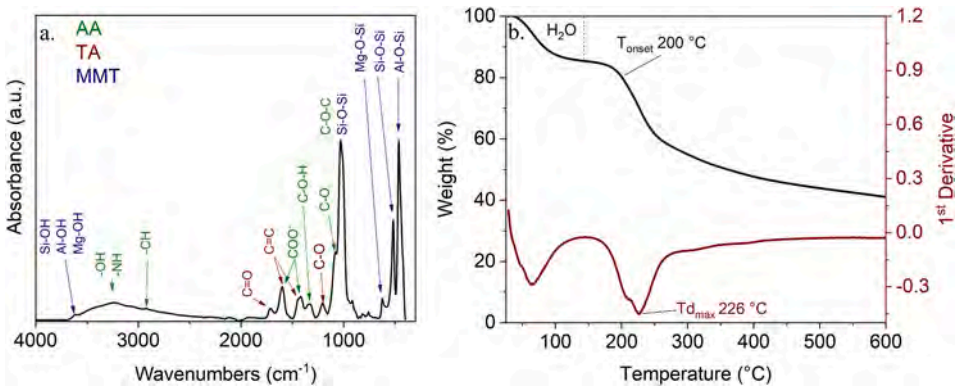

Fig. 3. (a) FTIR spectra recorded in attenuated total reflectance (ATR) mode, and (b) ThermoGravimetric Analysis (TGA), of the pristine aerogel.

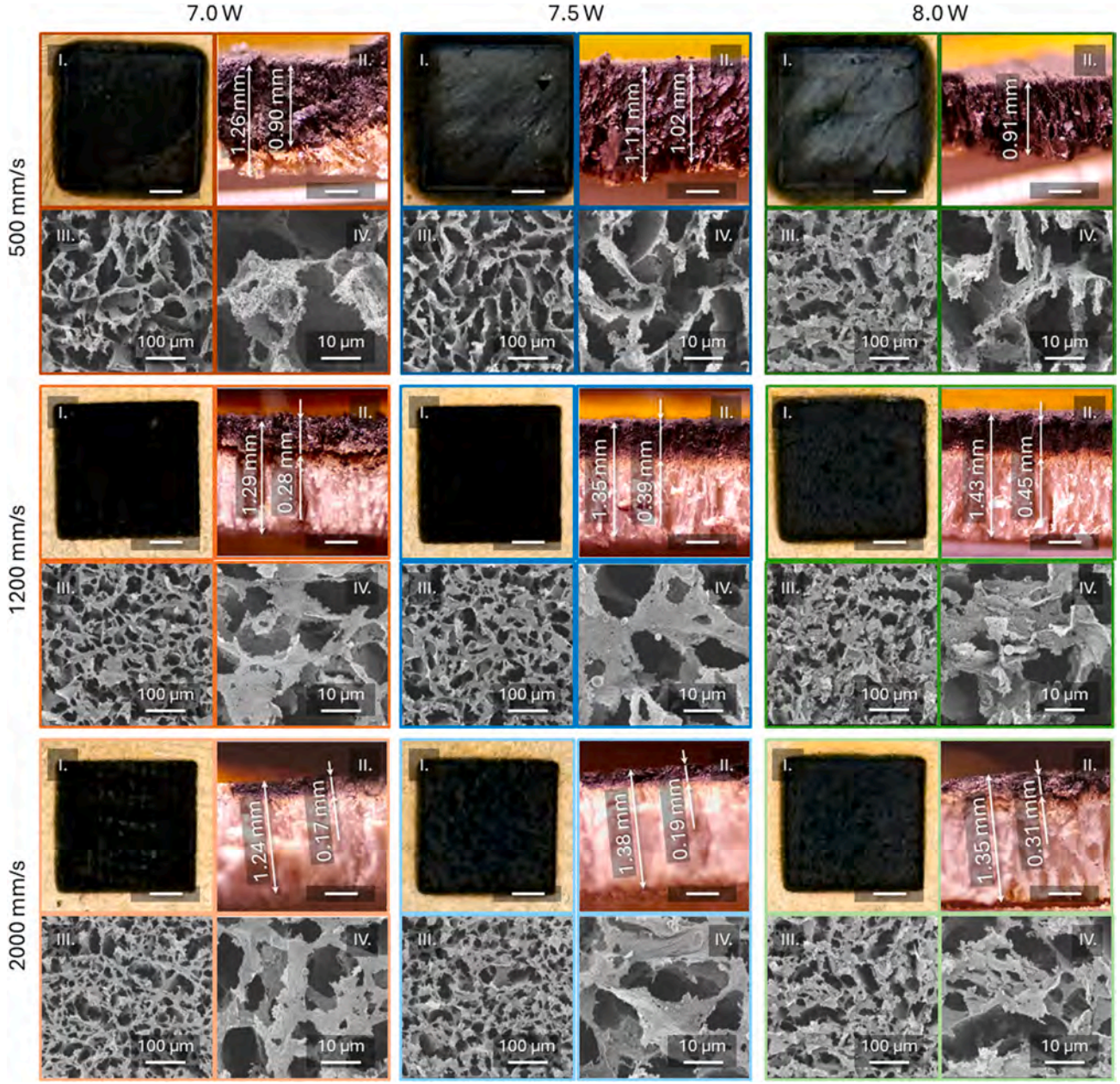

Fig. 4. Dosing tests performed on composite aerogel samples. Each panel of the rastering speed–power parameter matrix includes: (I) photograph of the sample after lasing (scale bar: 1 mm); (II) optical micrograph of the cross section (scale bar: 0.5 mm); (III) and (IV) SEM micrographs at 100 µm and 10 µm resolution, respectively.

pristine alginate, respectively, as previously reported [34]. Nevertheless, the aerogel remained stable up to 150 °C, exhibiting no phase transitions (melting, glass transition, or crystallization) below 80 °C (Fig. S.2).

3.2. Laser induced graphene characterization

The as-prepared composite aerogels were processed with an infrared CO_2 laser engraver ($\lambda = 10.6$ μm) under ambient atmosphere. Preliminary dosing tests indicated that this substrate is particularly suitable for LIG formation. The penetration depth of LIG was observed and measured in cross sections via optical microscopy (Fig. 4), showing a clear dependence on scanning speed and laser power. Notably, the penetration depth of LIG within the material is greater than that observed for polyimide [48] or other film-like substrates [49], likely due to the highly porous structure of the aerogel.

Morphological analysis was performed by SEM at multiple magnifications and is shown in Fig. 4. Examination of images acquired at 100 μm resolution confirms that the honeycomb structure of the pristine composite aerogel (Fig. 2) remains intact following laser processing in all examined samples. Slower scanning speeds correlate with the formation of larger pores due to the increased fluence delivered to the material surface, thus enhancing the gasification of oxygen-containing compounds. Consequently, samples processed at 1200 mm/s exhibit larger pores than those processed at 2000 mm/s, while samples irradiated at 500 mm/s showed the largest pores. Variation of laser power revealed similar morphology for 7 W and 7.5 W, whereas at 8 W it caused pronounced crumpling and collapse. High-magnification SEM images (10 μm resolution) reveal the presence of flake-like structures alongside rounded macroparticles (Fig. S.3a) of approximately 1 μm distributed throughout all samples. EDX analysis identified Si, Al and O as major elemental constituents of these macroparticles (Fig. S3b and table S.1), suggesting their origin as aluminosilicate particles derived from the MMT clay phase after high temperatures exposure (Fig. S3a).

The N_2 adsorption–desorption isotherms of the pristine and LIG samples are reported in Fig. S.1a. All samples display similar isotherm shapes, consistent with a type IV isotherm with an H3 hysteresis loop according to the IUPAC classification indicating the presence of not completely filled macropores [50]. While the micropore region remains almost unchanged, the most significant differences between the pristine aerogel and laser-treated samples are the formation of larger meso and macroporosities. This interpretation is further supported by the

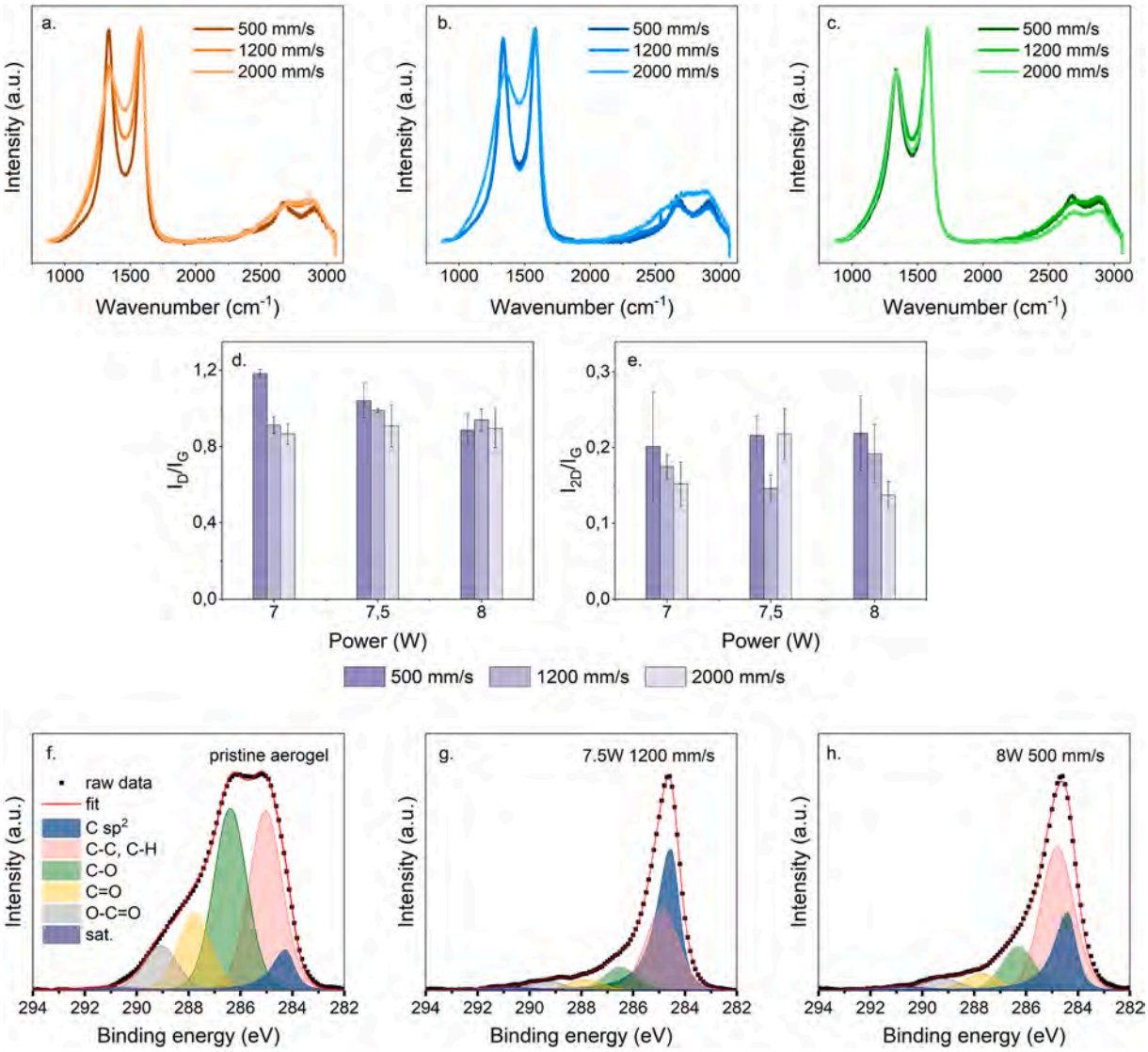

Fig. 5. Averaged Raman spectra over three samples of composite aerogels irradiated at scanning speeds of 500, 1200, and 2000 mm/s and laser powers of (a) 7.0 W, (b) 7.5 W, and (c) 8.0 W. (d) Averaged I_D/I_G and (e) I_{2D}/I_G ratios with error bars. HR C1s spectra of (f) pristine composite aerogel sample, and samples processed at (g) 7.5 W and 1200 mm/s and (h) 8.0 W and 500 mm/s.

Non-Local Density Functional Theory (NLDFT) analysis (Fig. S1b). The cumulative pore volume curve displays a pronounced increase below 50 nm, highlighting the crucial contribution of mesoporosity to the overall surface area. A further rise in the curve is observed around 70 nm, indicating that macropores also play a significant role in the pore structure. Among the LIG samples, the one prepared with slower scanning speed exhibits a larger meso and macropores' area, resulting in an increased specific surface area (max SSA = 14.03 ± 0.06 m^2/g for the sample obtained with 7.5 W and 500 mm/s). It should be noted that the reported SSA is calculated for the entire composite aerogel, which contains inert MMT clay (density 2.6 g/cm^3); the SSA of the LIG component alone would likely be higher, as carbons from low-density precursors generally exhibit higher surface area.

Raman spectra provide further insight into the transformation process (Fig. 5; deconvoluted spectra in Fig. S.4a). Graphene-derived carbon structures exhibit three prominent Raman features, as observable in the spectra of Fig. 5: the G band (~1580 cm^{-1}), which reflects the in-plane stretching vibration of sp^2-hybridized carbons [51]; the D band (~1350 cm^{-1}), associated with ring-breathing modes activated by lattice defects [39]; and the 2D band (~2700 cm^{-1}), representing the overtone of the D mode [37]. Additional features can also be resolved, as shown in Fig. S4a. At powers of 7–7.5 W and a writing speed of 2000 mm/s, the Raman spectra (Fig. 5a and b) reveal pronounced structural disorder, as evidenced by the broadening of the D and G bands and the presence of a single, unresolved second-order feature. The I_D/I_G ratio of ~0.9 is most likely attributable to insufficient energy input to promote the reorganization of sp^2 clusters into larger, well-ordered graphitic domains, as further indicated by the significant convolution between the D and G peaks. In contrast, at reduced scanning speeds of 500 and 1200 mm/s, the Raman spectra demonstrate the emergence of larger and more ordered graphitic domains. This is reflected by the clearer separation of the D and G bands and a progressive narrowing of their Full Width at Half Maximum (FWHM) with decreasing speed, consistent with the greater energy transferred into the material during the transformation process (Fig. S4b). Additional evidence of improved structural order is provided by the appearance of a more distinct 2D band, accompanied by reduced convolution from second-order combination modes. The I_D/I_G ratio (Fig. 5b) increases with rising fluence, shifting from values below 1 to values approaching or exceeding 1. This trend, together with the low FWHM values, indicates the formation of relatively large, ordered graphitic grains, while also suggesting defect generation induced by the higher energy density delivered to the material [52]. At 8 W, spectra in Fig. 5c, collected at different writing speeds, exhibit comparable features, namely broader D and G bands and a poorly defined second-order signal, all indicative of a defect-rich structure. The consistently similar I_D/I_G values (~0.9) under these conditions further support this conclusion. Moreover, the comparable FWHM values across all samples (130–140 cm^{-1} for the D band and 73–80 cm^{-1} for the G band) suggest that the observed defects arise not from incomplete material conversion into LIG, but rather from the excessive energy density delivered during processing [52]. Finally, the low I_{2D}/I_G ratios across all samples (0.14–0.22) are consistent with the formation of few-layer graphene-like structures (Fig. 5e) [53].

Taken together, SEM and Raman results reveal a coherent picture of the structural evolution. At 7–7.5 W and 500 mm/s, wider pores suggest pronounced degassing, consistent with the greater disorder observed in Raman spectra. At higher scan speeds, comparable morphologies are observed, with Raman features confirming LIG formation. Both analyses indicate that 7–7.5 W samples share similar characteristics, whereas 8 W results in more collapsed structures and spectra dominated by disorder-related grain features.

These findings were further confirmed by XPS analyses, performed on the pristine sample and on the samples lasered at 7.5 W - 1200 mm/s and at 8 W - 500 mm/s. Initial surveys confirmed the presence of the elements already detected by EDX analyses, with the addition of small amounts of sodium from the clay in the pristine sample. However, the survey already highlighted a significantly higher amount of carbonaceous material in the sample prepared at a laser power of 7.5 W and writing speed of 1200 mm/s (Table S.2). The High resolution (HR) C1s spectrum of the pristine aerogel sample (Fig. 5f) presented typical peaks related to its alginate and tannic acid components, with carbon atoms predominantly bound to oxygen groups [54–56]. However, once subjected to laser writing, the C1s spectrum is drastically reduced, confirming the successful conversion into partially ordered carbon structures in the sample written at 7.5 W and 1200 mm/s (Fig. 5g) with respect to the sample written at higher laser power (Fig. 5h). Indeed, in this sample it is possible to see a significant increase of the typical graphitic component at 284.5 eV, which was previously present in small quantities due to the tannic acid in the aerogel, and which now becomes the predominant peak of this spectrum, and of the small satellite peak at 291.3 eV. The deconvolution is then completed with the aliphatic peak at 285.0 eV, and a smaller component still oxidized as evidenced by the presence of the C-O, C=O and COOH peaks at 286.4 eV, 287.8 eV and 289.2 eV, respectively. Conversely, the sample subjected to higher power and lower writing speeds presents a more disordered carbon structure, as evidenced by the bigger aliphatic peak at 285.0 eV and a bigger peak related to C-O bonds [57].

3.3. Dye-sensitized solar cells

The physico-chemical characterisation of the prepared LIG/aerogel composites revealed how writing speed and power strongly affect the properties of the samples. Overall, this demonstrated the possibility of preparing a composite material that works both as a separator and as a porous, conductive electrode. Consequently, the prepared electrodes were tested in DSSCs. The devices were assembled so that the non-graphitized aerogel side faced the photoanode, avoiding short circuits and retaining the electrolyte, while the LIG side served as a catalytic counter electrode (Fig. 1a). Three writing conditions were chosen: 7.5 W 500 mm/s, 7.5 W 1200 mm/s, and 8 W 2000 mm/s. These were selected as the most relevant to study how the different LIG properties, including defects, surface area and writing depth, influenced device performance. For each writing condition, two DSSCs were prepared with different electrolytes. The first used MPN as the solvent, which is one of the most commonly used solvents when low volatility and long term stability are required [58–60]. The second used GVL, which our group recently reported as a more sustainable and less toxic solvent for DSSCs electrolyte, especially for indoor light illumination [61]. This test allowed to investigate how different solvent properties would impact the electrolyte behaviour within the hierarchical porous structure of the aerogel separator.

Fig. 6a presents the J-V characteristics of the DSSC recorded under simulated outdoor conditions (standard AM1.5G spectrum at 1 sun irradiance ~1000 W m^{-2}), and under simulated indoor conditions (calibrated CIE LED-B4 white light at 1000 lux–3 W m^{-2}). The J-V curves at 1 sun illumination revealed clear limitation for the fabricated devices under strong irradiance conditions, as confirmed by the photoconversion efficiency values below 1 % for all writing conditions. Nevertheless, for both solvents, a similar trend in device performance with respect to laser parameters was observed, providing relevant insights regarding the behaviour of these unprecedented composite materials in DSSC. The best photoconversion efficiencies were achieved with the LIG/aerogel composites obtained at 7.5 W and 500 mm/s, followed by the samples at 7.5 W and 1200 mm/s, with the worst performance achieved at 8W and 2000 mm/s. It is clear how this trend is strictly connected to the short circuit current density (J_{sc}) shown by the DSSC, while no explicit correlation was observed in the fill factor (FF) and open circuit voltage (V_{oc}) (Table S.3). Indeed, at 7.5 W and 500 mm/s, J_{sc} values of 3.3 and 2.1 mA/cm^2 were recorded for MPN and GVL, respectively. These values dropped to 0.28 and 0.6 mA/cm^2 for MPN and GVL using the electrodes made at 8 W and 2000 mm/s. These results are in line with the physico-chemical properties observed previously.

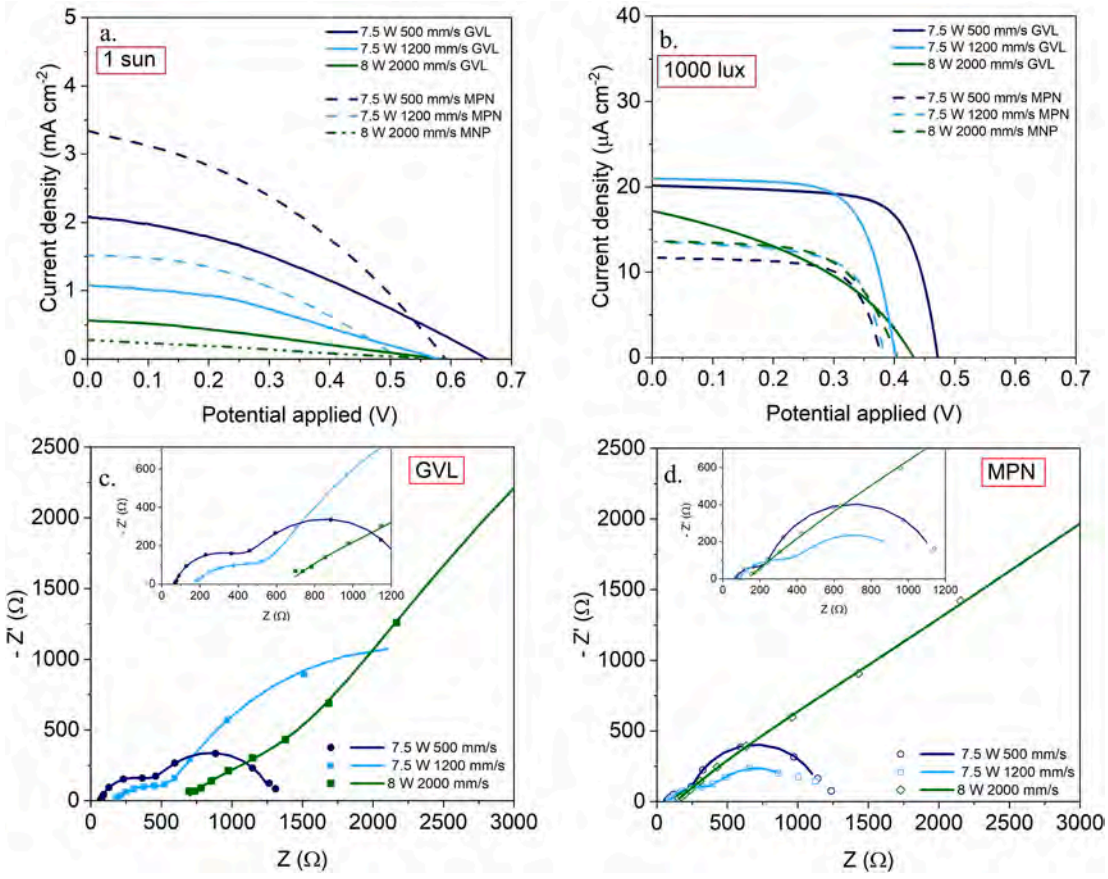

Fig. 6. (a) J–V curves of DSSCs with different tested electrodes and solvents (GVL and MPN) under 1 sun illumination; (b) J–V curves of the same cells under 1000 lux illumination; (c) electrochemical impedance spectroscopy (EIS) of cells with GVL; (d) EIS of cells with MPN.

The LIG/aerogel electrodes with the highest surface area (14.03 ± 0.06 m^2/g at 7.5W and 500 mm/s) are expected to enhance catalytic activity for triiodide reduction at the counter electrode, as the larger fraction of the aerogel converted to active LIG material provides more active sites [62]. Apart from catalytic area, the deeper penetration of the LIG within the aerogel structure also reduces the distance between the photoanode and the active material at the counter electrode, shortening the diffusion path for the electrolyte ions, allowing higher currents [61,63]. This is one of the reasons why the LIG/aerogel composites obtained at 2000 mm/s resulted in the worst performance, especially in terms of J_{sc}. Indeed, in this case the LIG thickness is roughly 0.3 mm while the portion of unconverted aerogel is higher than 1 mm (Fig. 4), which is extremely high compared with standard DSSC device assembly reported elsewhere [60,64]. The diffusion of the redox couple through the electrolyte becomes significant in this situation, limiting the J_{sc} and reducing device performances. In addition, the more defective LIG obtained under fast-writing conditions impacts the material resistivity and electrolyte diffusion.

Regarding the differences observed between the two solvents, the DSSC with the MPN-based electrolyte achieved the highest overall performances, especially in terms of photoconversion efficiency and J_{sc}. One of the reasons for this is the lower viscosity of MPN with respect to GVL, which facilitate ions diffusion within the electrolyte allowing higher current to flow within the DSSC [61]. On the other hand, all the DSSC with GVL-based electrolyte showed a higher V_{oc} with respect to the MPN counterparts. This evidence was already observed in the literature and has been associated, among other things, with the Lewis basicity of GVL, which promotes interaction with the uncovered TiO_2, shifting upward the surface energy levels thus enhancing V_{oc} [61,65], giving an effect similar to pyridine-based additives such as 4-tert-butylpyridine [66].

When the DSSCs were characterised under low intensity indoor illumination at 1000 lux (3 W m^{-2}), a significantly different behaviour emerged (Fig. 6b). Indeed, the correlation between laser writing conditions and device performance was less pronounced than under simulated sunlight. The much lower irradiance reduces the photogenerated current by two orders of magnitude, thereby diminishing the impact of limitations from lower counter electrode catalytic activity and ion diffusion associated with the higher interelectrode distance. Among the DSSC with the MPN-based electrolyte, the best performing device was still the one including the LIG/aerogel composite obtained at 7.5 W and 500 mm/s, with a photoconversion efficiency of 1.6 % (Table S.4). However, only a slightly lower photoconversion efficiency (1.1 %) was observed for the other two conditions (7.5 W, 1200 mm/s and 8 W, 2000 mm/s). In contrast, DSSCs using GVL as the solvent, particularly under 7.5 W 500 mm/s and 7.5 W 1200 mm/s, outperformed those with MPN in both Jsc and V_{oc}. Moreover, the 7.5 W 500 mm/s cell shows a remarkable increase in fill factor (0.72), and photoconversion efficiency (2.2 %), compared to the values shown under simulated sunlight illumination, equal to 0.34 and 0.5 %, respectively. This improvement aligns with the ability of GVL to improve the performance of DSSC under reduced indoor illumination conditions. Finally, the DSSC with GVL including the LIG/aerogel obtained at 8 W and 2000 mm/s showed a much lower FF (0.4), with respect to the other devices, due to a strong and unexpected resistive behaviour clearly visible in Fig. 6b.

Further insight into the electrical and electrochemical processes impacting the device performances both under simulated outdoor and indoor conditions were obtained performing EIS measurements of the prepared DSSCs. Fig. 6c and d shows the Nyquist plot of the GVL and MPN cells, respectively, under dark conditions and with an applied bias

of 0.6 V, including the measured experimental values and the results of the fitting performed with the equivalent circuit shown in Fig. S.5. Here, R_s represents the series resistance; $R_{CE}//Q_{CE}$, corresponds to the charge transfer at the counter electrode; $R_r//Q_\mu$, represents the recombination processes at the photoanode (Fig. S5 description) [66]. EIS measurements provide further confirmation of the observations made previously, based on the JV measurements. In particular, R_s and the R_{CE} clearly depend on the writing conditions (Table S.5). For the MPN-based DSSC, the sample at 7.5 W and 500 mm/s exhibits a lower R_s (70 Ω) due to a less defective and more conductive LIG structure. This effect is evident also from the low FF recorded under outdoor conditions, where ohmic losses are more visible due to higher generated currents. In the worst case (8 W 2000 mm/s) the R_s is so high that the reduced FF effect is visible even under low illumination, where the photogenerated current is much lower and resistive behaviour in series are normally less impactful. A similar trend can be observed looking at the R_{CE}: in MPN-based DSSC, the lowest value of 169 Ω is measured at 7.5 W and 500 mm/s, while strongly increased to 4112 Ω at 8 W and 2000 mm/s. This confirms that a higher surface area and a larger volume of active material reduce the resistance for triiodide catalytic reduction. The same trend was observed for the GVL-based DSSC, with values of R_s and R_{CE} values that were overall higher with respect to the MPN-based counterparts, consistent with previous observations [61].

The presented and discussed data confirm the potential of this substrate to serve as a catalytic counter-electrode for DSSCs, particularly under indoor illumination, and highlight its suitability as a low-cost material for sensors and Internet of Things applications. However, the obtained cell efficiency is still low (~2 %). Nevertheless, two important factors must be considered. The first one is the already discussed thickness of the aerogel (~1 mm). Although most of the aerogel is converted into LIG, the total thickness can still influence cell performances. The second factor is the specific surface area (SSA). The best result obtained in this work showed an SSA of only 14 m^2/g. This value is remarkably low compared to other carbon-based electrodes, such as activated carbon [67], which can reach ~1950 m^2/g, and even biobased carbons, clearly highlighting the very limited surface area of our material [68,69].

For these reasons, the best results were compared with three different cell configurations. In the first two, a conventional Pt counter-electrode was used: one with the aerogel as a separator, and the other sealed without a separator but maintaining the same electrode distance as the aerogel thickness. These setups enable to distinguish the catalytic activity of the counter electrode from the effects of inter-electrode spacing and geometry. In the third configuration, an activated carbon (AC) and carbon black composite ink was deposited onto the aerogel by doctor blade to compare a high-surface-area carbon material with LIG, evaluating the relationship between surface area and catalytic activity under identical electrode spacing.

From J–V curves of these cells (Fig. 7), it is evident that the best performance under all tested conditions was obtained when AC-based ink was deposited on the aerogel. This cell performed comparably to the cell containing free liquid electrolyte using a Pt counter-electrode, except for a higher V_{oc} observed for AC cell (Table S.6). This increased V_{oc} can be attributed to a lower recombination as it has been already demonstrated that the high surface area and the porous structure are beneficial for ionic transport minimizing the undesired reactions [62,68,70].

Surprisingly, the LIG cell and the cell with a Pt counter-electrode

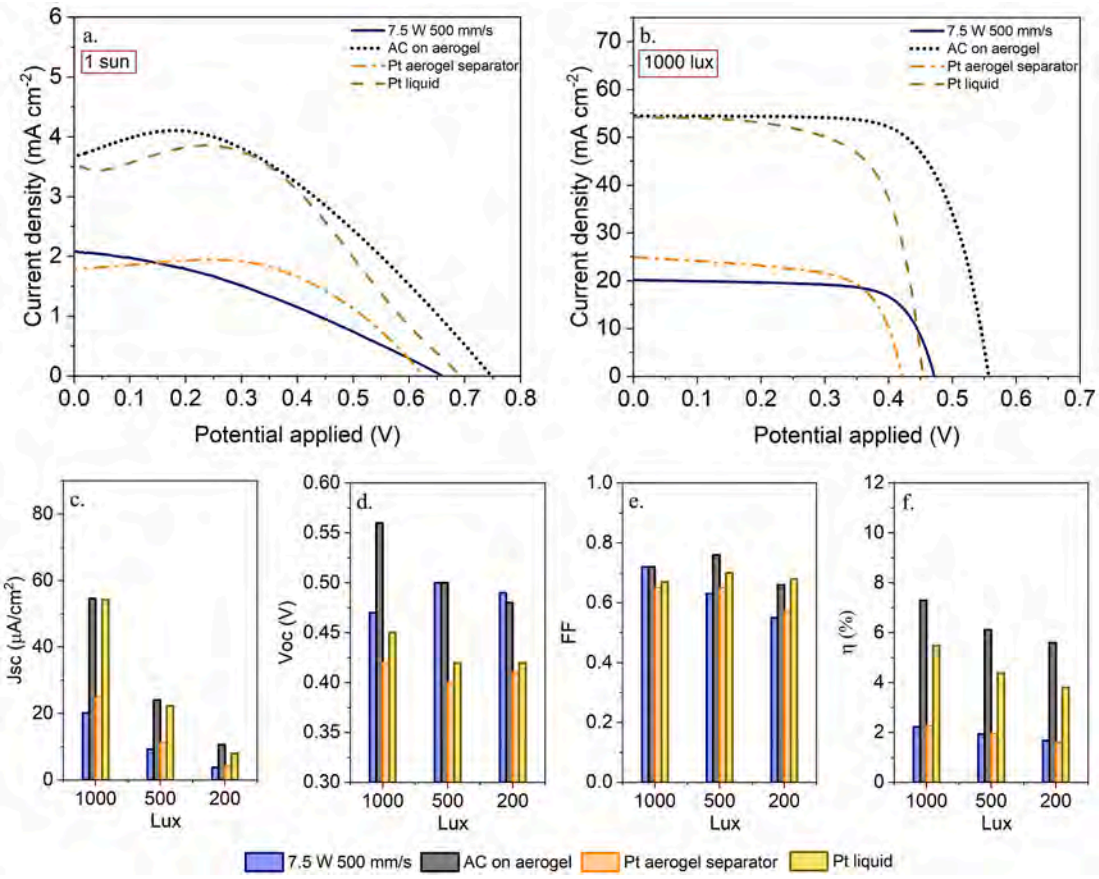

Fig. 7. (a) J–V curves of DSSCs with different electrodes and cell configurations under 1 sun illumination; (b) J–V curves of the same cells under indoor illumination; (c) short-circuit current density (Jsc), (d) open-circuit voltage (V_{oc}), (e) fill factor (FF), and (f) power conversion efficiency (PCE) of the cells measured at three indoor illumination levels (1000, 500, and 200 lux).

sealed using aerogel as an electrolyte scaffold exhibit almost identical behaviour. Even though under outdoor conditions the Pt-based cell shows a higher FF and overall efficiency, under indoor illuminations the device characteristics of the two cells are very similar, with the carbon-based LIG electrode, displaying a higher V_{oc} and FF (Fig. 7d and e). These findings confirm that, with the same cell geometry, the LIG electrode exhibits interesting and promising catalytic properties. The structure of the obtained LIG, which maintains the structural anisotropy of the aerogel precursor, may have contributed to improved performance by compensating for the overall SSA of the LIG-inorganic composite material, which is much lower than other carbonaceous materials such as AC [71]. This suggests that the internal anisotropic structure is a crucial asset of the material, leading to cell performances comparable to that of platinum electrodes under the same cell geometry conditions. By appropriately modifying the substrate, in terms of thickness and surface area, and increasing microporosities (easily achieved using alternative aerogel synthesis techniques such as supercritical drying), significant improvements in performance are expected.

3.4. Supercapacitor

Based on Raman, XPS and SEM analyses, the optimal laser-writing parameters were determined to be a power of 7.5 W and a scanning speed of 1200 mm/s. Under these conditions, the material exhibited a trade-off between short range order and amorphous content (Fig. 5b) while preserving the pristine aerogel structure (Fig. 4). Under these conditions, carbon materials are expected to show capacitive performances controlled by the long-range disordered structure while preserving an overall multilayer graphene structure typical of LIG [72]. In other conditions, we demonstrated the material not to be referred to as LIG but rather amorphous carbons [73]. These parameters were therefore selected for evaluating the charge storage performance in the supercapacitor (SC). The ionic liquid [PYR14][TFSI] was selected as electrolyte since ionic liquid-based SCs demonstrated average state-of-the-art areal energy and power densities, excellent coulombic efficiency and specific capacitance, while maintaining negligible volatility, low flammability, and chemical stability [74].

Fig. 8a shows the results of the three-electrode characterization under anodic and cathodic scans for the determination of the device voltage and, consequently, the areal charge balancing. The analysis revealed a symmetric potential window with respect to the OCP. The cutoff potentials selected in anodic and cathodic polarizations correspond to the absolute deviation from OCP, enabling the use of a 1.6 V operating range. The criterion for selecting the polarization limits was based on the coulombic efficiency trends traded with the observable evolution of electrolysis currents towards the polarization limits. The calculated electrode area ratio S_+/S_- is close to unity, confirming that the two electrodes possess the same specific capacity. After optimization, a symmetric sandwich-type device was fabricated by assembling two electrodes with an active area of 48 mm^2 each and employing [PYR14][TFSI] as electrolyte. The Nyquist plot of the full device is presented in Fig. 8b. The equivalent circuit used to fit the Nyquist plot and the fitting results are reported in Fig. S.6 and Table S.7, respectively. Electrochemical capacitors can be modelled as an ideal capacitor in series with an equivalent series resistance (ESR). In this case, a semicircle is also observed in the Nyquist plot, a feature characteristic of carbon-based electrodes. This high-frequency semicircle is generally attributed to limited electronic conductivity between carbon particles and imperfect contact between the electrode material and the current collector [75,76]. At low frequencies, the spectrum displays a nearly vertical trend of the imaginary component, characteristic of capacitive systems. These findings confirm the capacitive nature of the material, while also highlighting a significant resistive contribution, most likely associated with its highly porous morphology typical of aerogels. CVs were performed at scan rates ranging from 5 to 200 mV/s with quasi-logarithmic increments (Fig. 8c). This range was selected to assess the rate capability of the material, allowing for the evaluation of its performance at different charge-discharge rates (Fig. S.7a) The CV curves exhibit a nearly rectangular shape, characteristic of electric double-layer capacitors (EDLCs), retained even at high scan rates. Galvanostatic charge–discharge (GCD) measurements further corroborated the purely capacitive storage mechanism, displaying triangular profiles with negligible IR drops at low current densities (Fig. 8d). GCD tests were conducted at current densities from 5 to 200 $\mu A/cm^2$. These current densities were chosen to further investigate the material rate capability. From these measurements, areal capacitance values were extracted (Fig. S7b), reaching a maximum of 1.49 mF/cm^2 at low current densities, consistent with other symmetric EDLC devices employing LIG electrodes derived from sustainable precursors [19,77]. The Ragone plot demonstrates that composite aerogel-derived LIG achieves energy and power density characteristics comparable or slightly higher than SCs fabricated using LIG from other green substrates (Fig. 8e). A further comparison of key performance parameters for SCs employing laser-fabricated electrodes on both sustainable and non-sustainable substrates is provided in Fig. S.8 and Table S.8.

4. Conclusions

In this work, a renewable-resource-derived aerogel with highly oriented porosity (97.2 ± 0.3 %) was employed as the substrate for LIG formation, yielding a material in which the anisotropic architecture of the pristine aerogel was preserved after laser processing. The results demonstrate that laser scan speed has a pronounced influence on pore morphology and structural order. Lower speeds lead to larger pores and higher surface areas (up to14.03 ± 0.06 m^2/g), while Raman and XPS analyses revealed that reduced scan speeds (500–1200 mm/s) promote graphitic ordering. In contrast, higher power (8 W) induces structural collapse and defect generation. Among the tested DSSCs, the best performance was achieved with electrodes fabricated at 7.5 W and 500 mm/s, via enhanced surface area, penetration depth, and reduced inter-electrode spacing. When using GVL as the solvent, cells illuminated at 1000 lux exhibited a marked improvement in fill factor (0.72) and photoconversion efficiency (2.2 %) compared to simulated outdoor conditions (0.34 and 0.5 %, respectively), confirming its indoor suitability. The main limitations remain cell geometry, inter-electrode distance, and moderate surface area; crucially, at identical geometry, LIG matches Pt performance while delivering higher Voc, as expected for carbon-based electrodes. These findings highlight the potential of the obtained material, whose anisotropic structure may enhance active surface utilization and partially offset surface area constraints. For supercapacitor applications, aerogel-derived LIG electrodes displayed characteristic EDLC behaviour, with Nyquist plots showing finite resistance and near-vertical low-frequency regions, rectangular CV profiles even at high scan rates, and triangular GCD curves with minimal IR drop. The areal capacitance reached 1.49 mF/cm^2 at low current densities, and the Ragone analysis confirmed energy and power densities comparable to or exceeding those of other sustainable LIG-based EDLCs. Overall, the aerogel composed of tannic acid, alginate, and montmorillonite demonstrated excellent laser-writing compatibility and promising multifunctionality for both energy harvesting and storage. Future work should focus on optimizing the formulation while maintaining the anisotropic framework, particularly through control of substrate thickness and increase of surface area, for example via supercritical drying.

CRediT authorship contribution statement

S. Amenta: Writing – original draft, Visualization, Investigation, Formal analysis, Conceptualization. **A. Bisceglie:** Writing – original draft, Visualization, Investigation, Formal analysis, Conceptualization. **R. Speranza:** Writing – review & editing, Visualization, Validation, Supervision, Methodology, Formal analysis, Conceptualization. **S. Martellone:** Writing – original draft, Investigation. **P. Zaccagnini:**

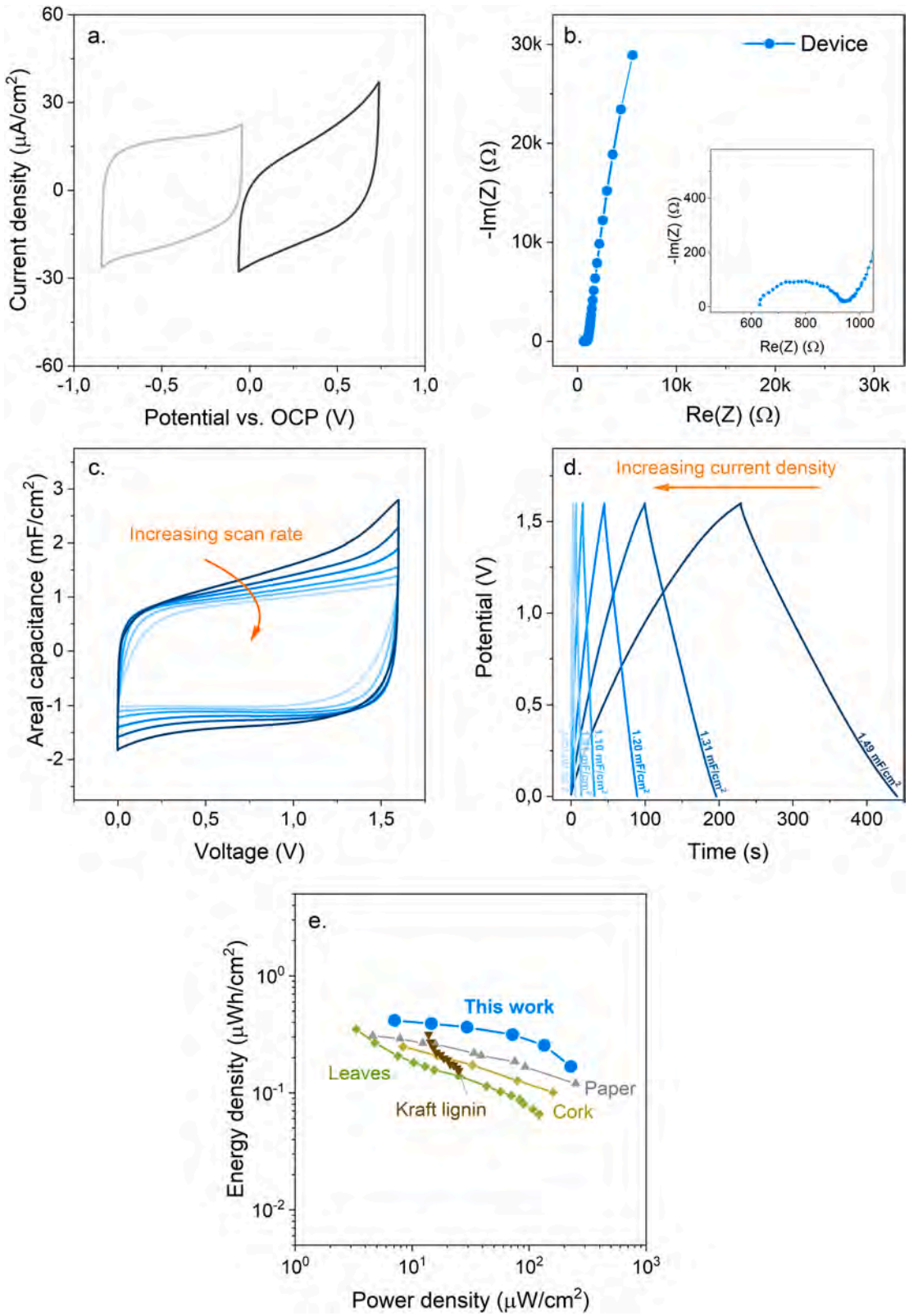

Fig. 8. (a) CV curves of anodic (dark grey) and cathodic (light grey) polarization tests performed in three-electrode configuration at 5 mV/s; (b) Nyquist plot of the assembled device; (c) CV curves within the optimized potential window at scan rates from 5 to 200 mV/s, with colour scale from dark to light corresponding to increasing scan rate (quasi-logarithmic progression); (d) GCD profiles at current densities from 5 to 200 μA/cm^2, with color scale from dark to light corresponding to increasing current density (quasi-logarithmic progression). Extracted areal capacitance values are indicated on the corresponding curve; (e) Ragone plot derived from GCD data and compared with literature reports on LIG-based supercapacitors from green precursors [19,25,78,79].

Writing – review & editing, Validation, Supervision, Project administration, Methodology, Formal analysis, Conceptualization. **L. Baudino:** Investigation, Writing – original draft. **J. Gómez-Monterde:** Validation, Formal analysis. **L. Marchese:** Funding acquisition, Supervision, Writing – review & editing. **M. Sànchez-Soto:** Writing – review & editing, Validation, Supervision, Methodology, Funding acquisition. **A. Lamberti:** Writing – review & editing, Validation, Supervision, Project administration, Funding acquisition.

Availability of data

All data are available on request from the corresponding author.

Declaration of competing interest

The authors declare that they have no known competing financial interests or personal relationships that could have appeared to influence the work reported in this paper.

Acknowledgement

This publication was partially funded under the National Recovery and Resilience Plan (NRRP), Mission 4 "*Education and Research*"—Component 2 "*From research to business*"—Investment 3.3 "*Introduction of innovative doctorates that meet the innovation needs of companies and promote the hiring of researchers by companies*", through Ministerial Decree no. 352 of April 9, 2022. This article was also partially funded under the National Recovery and Resilience Plan (NRRP), Mission 4 "Education and Research"—Component 2 "From research to business"— Investment 3.1 "Fund for the realization of an integrated system of research and innovation infrastructures"—Call for tender No. n. 3264 of December 28, 2021 of Italian Ministry of Research funded by the European Union—NextGenerationEU—Project code: IR0000027, Concession Decree No. 128 of June 21, 2022 adopted by the Italian Ministry of Research, CUP: B33C22000710006, Project title: iENTRANCE. This work was partially funded by the project "nuovi Concetti, mAteriali e tecnologie per l'iNtegrazione del fotoVoltAico negli edifici e in uno scenario di generazione diffuSa" ("CANVAS"), funded by the Italian Ministry of the Environment and the Energy Security, through the Research Fund for the Italian Electrical System (type-A call, published on G.U.R.I. n. 192 on 18-08-2022). This result is part of a project that has received funding from the European Research Council (ERC) under the European Union's ERC Starting Grant agreement "CO2CAP" No. 949916. This manuscript reflects only the authors' views and opinions, neither the European Union nor the European Commission can be considered responsible for them. Miguel Sánchez-Soto acknowledges the EcoPolyRub Project: PID2023-151338NB-I00, funded by the Ministry of Science, Innovation and Universities, the State Research Agency, and the European Regional Development Fund (FEDER). Also acknowledges the support received from the Generalitat of Catalonia through the project 2021SGR01042. The authors would also like to acknowledge PRIN CARE - CO2 Advanced, environmental-friendly nano-technology based REduction (CARE).

Appendix A. Supplementary data

Supplementary data to this article can be found online at https://doi.org/10.1016/j.jpowsour.2026.239495.

Data availability

Data will be made available on request.

References

[1] K.S. Novoselov, A.K. Geim, S.V. Morozov, et al., Electric Field Effect in Atomically Thin Carbon Films, vol.404, Kluwer, 2004, https://doi.org/10.1126/science.1102896.
[2] Z. Sun, S. Fang, Y.H. Hu, 3D graphene materials: from understanding to design and synthesis control, Chem Rev 120 (2020) 10336–10453, https://doi.org/10.1021/acs.chemrev.0c00083.
[3] A.B. Bourlinos, V. Georgakilas, R. Zboril, et al., Aqueous-phase exfoliation of graphite in the presence of polyvinylpyrrolidone for the production of water-soluble graphenes, Solid State Commun. 149 (2009) 2172–2176, https://doi.org/10.1016/j.ssc.2009.09.018.
[4] Y. Hernandez, V. Nicolosi, M. Lotya, et al., High-yield production of graphene by liquid-phase exfoliation of graphite, Nat. Nanotechnol. 3 (2008) 563–568, https://doi.org/10.1038/nnano.2008.215.
[5] S. Park, R.S. Ruoff, Chemical methods for the production of graphenes, Nat. Nanotechnol. 4 (2009) 217–224, https://doi.org/10.1038/nnano.2009.58.
[6] R. Ye, D.K. James, J.M. Tour, Laser-induced graphene: from discovery to translation, Adv. Mater. 31 (2019), https://doi.org/10.1002/adma.201803621.
[7] B. Qi, K. Ren, Y. Lin, et al., Design of layered-stacking graphene assemblies as advanced electrodes for supercapacitors, Particuology 60 (2022) 1–13, https://doi.org/10.1016/j.partic.2021.03.001.
[8] Y. Liu, P. Liu, L. Li, et al., Fabrication of biomass-derived activated carbon with interconnected hierarchical architecture via H3PO4-assisted KOH activation for high-performance symmetrical supercapacitors, J. Electroanal. Chem. 903 (2021), https://doi.org/10.1016/j.jelechem.2021.115828.
[9] M. Wu, Q. Zha, J. Qiu, et al., Preparation and characterization of porous carbons from PAN-based preoxidized cloth by KOH activation, Carbon N Y 42 (2004) 205–210, https://doi.org/10.1016/j.carbon.2003.10.025.
[10] M. Jafari, G.G. Botte, Sustainable green route for activated carbon synthesis from biomass waste for high-performance supercapacitors, ACS Omega (2023), https://doi.org/10.1021/acsomega.3c09438.
[11] C. Zhang, W. Lv, Y. Tao, et al., Towards superior volumetric performance: design and preparation of novel carbon materials for energy storage, Energy Environ. Sci. 8 (2015) 1390–1403, https://doi.org/10.1039/c5ee00389j.
[12] F. Wang, X. Mei, K. Wang, et al., Rapid and low-cost laser synthesis of hierarchically porous graphene materials as high-performance electrodes for supercapacitors, J. Mater. Sci. 54 (2019) 5658–5670, https://doi.org/10.1007/s10853-018-03247-0.
[13] K. Avinash, F. Patolsky, Laser-induced graphene structures: from synthesis and applications to future prospects, Mater. Today 70 (2023) 104–136, https://doi.org/10.1016/j.mattod.2023.10.009.
[14] J. Lin, Z. Peng, Y. Liu, et al., Laser-induced porous graphene films from commercial polymers, Nat. Commun. 5 (2014), https://doi.org/10.1038/ncomms6714.
[15] S. Bai, Y. Tang, L. Lin, et al., Investigation of micro/nano formation mechanism of porous graphene induced by CO2 laser processing on polyimide film, J. Manuf. Process. 84 (2022) 555–564, https://doi.org/10.1016/j.jmapro.2022.10.037.
[16] C. Song, M. Guan, Y. Jia, et al., Driving forces for ultrafast laser-induced sp2 to sp3 structural transformation in graphite, npj Comput. Mater. 9 (2023), https://doi.org/10.1038/s41524-023-01035-2.
[17] M. Reina, A. Scalia, G. Auxilia, et al., Boosting electric double layer capacitance in laser-induced graphene-based supercapacitors, Adv. Sustain. Syst. 6 (2022), https://doi.org/10.1002/adsu.202100228.
[18] W. Ma, J. Zhu, Z. Wang, et al., Recent advances in preparation and application of laser-induced graphene in energy storage devices, Mater. Today Energy 18 (2020), https://doi.org/10.1016/j.mtener.2020.100569.
[19] F. Mahmood, F. Mahmood, H. Zhang, et al., Laser-induced graphene derived from kraft lignin for flexible supercapacitors, ACS Omega 5 (2020) 14611–14618, https://doi.org/10.1021/acsomega.0c01293.

[20] D. Butler, V. Kammarchedu, K. Zhou, et al., Cellulose-based laser-induced graphene devices for electrochemical monitoring of bacterial phenazine production and viability, Sensor. Actuator. B Chem. 378 (2023), https://doi.org/10.1016/j.snb.2022.133090.
[21] M.J. Nine, D.N.H. Tran, T.T. Tung, et al., Graphene-borate as an efficient fire retardant for cellulosic materials with multiple and synergetic modes of action, ACS Appl. Mater. Interfaces 9 (2017) 10160–10168, https://doi.org/10.1021/acsami.7b00572.
[22] T. Pinheiro, R. Correia, M. Morais, et al., Water peel-off transfer of electronically enhanced, paper-based laser-induced graphene for wearable electronics, ACS Nano 16 (2022) 20633–20646, https://doi.org/10.1021/acsnano.2c07596.
[23] H.R. Moon, B. Ryu, Review of laser-induced graphene (LIG) produced on eco-friendly substrates, International Journal of Precision Engineering and Manufacturing - Green Technology 11 (2024) 1279–1294, https://doi.org/10.1007/s40684-024-00595-y.
[24] T. Vićentić, I. Greco, C.S. Iorio, et al., Laser-induced graphene on cross-linked sodium alginate, Nanotechnology 35 (2024), https://doi.org/10.1088/1361-6528/ad143a.
[25] T.S.D. Le, Y.A. Lee, H.K. Nam, et al., Green flexible Graphene–inorganic-hybrid micro-supercapacitors made of fallen leaves enabled by ultrafast laser pulses, Adv. Funct. Mater. 32 (2022), https://doi.org/10.1002/adfm.202107768.
[26] H.B. Chen, Y.Z. Wang, M. Sánchez-Soto, et al., Low flammability, foam-like materials based on ammonium alginate and sodium montmorillonite clay, Polymer (Guildf.) 53 (2012) 5825–5831, https://doi.org/10.1016/j.polymer.2012.10.029.
[27] C.H. Dreimol, H. Guo, M. Ritter, et al., Sustainable wood electronics by iron-catalyzed laser-induced graphitization for large-scale applications, Nat. Commun. 13 (2022), https://doi.org/10.1038/s41467-022-31283-7.
[28] P. Zhao, C. Liang, Y. Zhang, et al., Upgrading renewable natural tannic acid to multifunctional graphene-based materials by direct laser writing, J. Anal. Appl. Pyrolysis 186 (2025), https://doi.org/10.1016/j.jaap.2024.106927.
[29] K.D. Kumar, Y.A. Kumar, T. Ramachandran, et al., Cactus-like Ni-Co/CoMn2O4 composites on Ni foam: unveiling the potential for advanced electrochemical materials for pseudocapacitors, Mater. Sci. Eng., B 296 (2023), https://doi.org/10.1016/j.mseb.2023.116715.
[30] L. Borchardt, M. Oschatz, S. Kaskel, Tailoring porosity in carbon materials for supercapacitor applications, Mater. Horiz. 1 (2014) 157–168, https://doi.org/10.1039/c3mh00112a.
[31] X. Ji, Y. Zhong, C. Li, et al., Nanoporous carbon aerogels for laser-printed wearable sensors, ACS Appl. Nano Mater. 4 (2021) 6796–6804, https://doi.org/10.1021/acsanm.1c00858.
[32] R. Speranza, M. Reina, P. Zaccagnini, et al., Laser-induced graphene as a sustainable counter electrode for DSSC enabling flexible self-powered integrated harvesting and storage device for indoor application, Electrochim. Acta 460 (2023), https://doi.org/10.1016/j.electacta.2023.142614.
[33] P. Zaccagnini, A. Lamberti, A perspective on laser-induced graphene for micro-supercapacitor application, Appl. Phys. Lett. 120 (2022), https://doi.org/10.1063/5.0078707.
[34] L.G. De la Cruz, T. Abt, N. León, et al., Radially and axially oriented ammonium alginate aerogels modified with clay/tannic acid and crosslinked with glutaraldehyde, Gels 10 (2024), https://doi.org/10.3390/gels10080526.
[35] Z.E. Brubaker, J.J. Langford, R.J. Kapsimalis, et al., Quantitative analysis of raman spectral parameters for carbon fibers: practical considerations and connection to mechanical properties, J. Mater. Sci. 56 (2021) 15087–15121, https://doi.org/10.1007/s10853-021-06225-1.
[36] Z.E. Brubaker, A. Miskowiec, J.L. Niedziela, Raman spectroscopy of thermally perturbed carbon fibers: discriminating spectral responses of modulus classes and defect types, Phys. Rev. Mater. 6 (2022), https://doi.org/10.1103/PhysRevMaterials.6.073603.
[37] S. Claramunt, A. Varea, D. López-Díaz, et al., The importance of interbands on the interpretation of the raman spectrum of graphene oxide, J. Phys. Chem. C 119 (2015) 10123–10129, https://doi.org/10.1021/acs.jpcc.5b01590.
[38] D. López-Díaz, M. López Holgado, J.L. García-Fierro, et al., Evolution of the raman spectrum with the chemical composition of graphene oxide, J. Phys. Chem. C 121 (2017) 20489–20497, https://doi.org/10.1021/acs.jpcc.7b06236.
[39] A. Sadezky, H. Muckenhuber, H. Grothe, et al., Raman microspectroscopy of soot and related carbonaceous materials: spectral analysis and structural information, Carbon N Y 43 (2005) 1731–1742, https://doi.org/10.1016/j.carbon.2005.02.018.
[40] N. Fairley, V. Fernandez, M. Richard-Plouet, et al., Systematic and collaborative approach to problem solving using X-ray photoelectron spectroscopy, Appl. Surf. Sci. Adv. 5 (2021), https://doi.org/10.1016/j.apsadv.2021.100112.
[41] P.W. Ruch, D. Cericola, M. Hahn, et al., On the use of activated carbon as a quasi-reference electrode in non-aqueous electrolyte solutions, J. Electroanal. Chem. 636 (2009) 128–131, https://doi.org/10.1016/j.jelechem.2009.09.007.
[42] Y. Ma, J. Zhu, H. He, et al., Infrared investigation of organo-montmorillonites prepared from different surfactants, Spectrochim. Acta Mol. Biomol. Spectrosc. 76 (2010) 122–129, https://doi.org/10.1016/j.saa.2010.02.038.
[43] T. Wahyono, D.A. Astuti, Gede Wiryawan I. Komang, et al., Fourier transform Mid-Infrared (FTIR) spectroscopy to identify tannin compounds in the panicle of sorghum mutant lines, in: IOP Conf Ser Mater Sci Eng, Institute of Physics Publishing, 2019, https://doi.org/10.1088/1757-899X/546/4/042045 vol. 546.
[44] X. Zou, J. Huang, Hydrogen bond-regulated rapid prototyping and performance optimization of polyvinyl alcohol–tannic acid hydrogels, Gels 11 (2025), https://doi.org/10.3390/gels11080602.
[45] H. Li, C. Liu, J. Sun, et al., Bioactive edible sodium alginate films incorporated with tannic acid as antimicrobial and antioxidative food packaging, Foods 11 (2022), https://doi.org/10.3390/foods11193044.
[46] A. Sharma, C. Verma, S. Mukhopadhyay, et al., Development of sodium alginate/glycerol/tannic acid coated cotton as antimicrobial system, Int. J. Biol. Macromol. 216 (2022) 303–311, https://doi.org/10.1016/j.ijbiomac.2022.06.168.
[47] M. Sakizci, B. Erdoğan Alver, Ö. Alver, et al., Spectroscopic and thermal studies of bentonites from Ünye, Turkey, J. Mol. Struct. 969 (2010) 187–191, https://doi.org/10.1016/j.molstruc.2010.02.008.
[48] M.G. Stanford, C. Zhang, J.D. Fowlkes, et al., High-resolution laser-induced graphene. Flexible electronics beyond the visible limit, ACS Appl. Mater. Interfaces 12 (2020) 10902–10907, https://doi.org/10.1021/acsami.0c01377.
[49] P. Zaccagnini, C. Ballin, M. Fontana, et al., Laser-induced graphenization of PDMS as flexible electrode for microsupercapacitors, Adv. Mater. Interfac. 8 (2021), https://doi.org/10.1002/admi.202101046.
[50] M. Thommes, K. Kaneko, A.V. Neimark, et al., Physisorption of gases, with special reference to the evaluation of surface area and pore size distribution (IUPAC technical report), Pure Appl. Chem. 87 (2015) 1051–1069, https://doi.org/10.1515/pac-2014-1117.
[51] A.C. Ferrari, D.M. Basko, Raman spectroscopy as a versatile tool for studying the properties of graphene, Nat. Nanotechnol. 8 (2013) 235–246, https://doi.org/10.1038/nnano.2013.46.
[52] A. Velasco, Y.K. Ryu, A. Hamada, et al., Laser-induced graphene microsupercapacitors: structure, quality, and performance, Nanomaterials 13 (2023), https://doi.org/10.3390/nano13050788.
[53] J Bin Wu, M.L. Lin, X. Cong, et al., Raman spectroscopy of graphene-based materials and its applications in related devices, Chem. Soc. Rev. 47 (2018) 1822–1873, https://doi.org/10.1039/c6cs00915h.
[54] A. Jejurikar, X.T. Seow, G. Lawrie, et al., Degradable alginate hydrogels crosslinked by the macromolecular crosslinker alginate dialdehyde, J. Mater. Chem. 22 (2012) 9751–9758, https://doi.org/10.1039/c2jm30564j.
[55] C. Wang, P.X. Hou, Y. Zhao, et al., Tannic acid coated single-wall carbon nanotube membranes for the recovery of Au from trace-level solutions, Nano Res. 16 (2023) 11350–11357, https://doi.org/10.1007/s12274-023-5803-y.
[56] T. Bunwong, T. Siripongpreda, R. Nuisin, Sustainable metal-phenolic hybrid adsorbent: double-Crosslinked alginate/carboxymethyl cellulose for effective ammonium ion capture, Int. J. Biol. Macromol. 331 (2025), https://doi.org/10.1016/j.ijbiomac.2025.148347.
[57] M.C. Biesinger, Accessing the robustness of adventitious carbon for charge referencing (correction) purposes in XPS analysis: insights from a multi-user facility data review, Appl. Surf. Sci. 597 (2022), https://doi.org/10.1016/j.apsusc.2022.153681.
[58] R. Speranza, P. Zaccagnini, A. Scalia, et al., Pouch-sealing as an effective way to fabricate flexible dye-sensitized solar cells and their integration with supercapacitors, J. Power Sources 583 (2023), https://doi.org/10.1016/j.jpowsour.2023.233581.
[59] M. Agliuzza, R. Speranza, A. Lamberti, et al., Experimental and modeling study for the solar-driven CO2 electrochemical reduction to CO, Appl. Sci. 15 (2025), https://doi.org/10.3390/app15020549.
[60] F. Santos, D. Ivanou, A.M. Mendes, Boosting the performance of monolithic dye-sensitized solar cells under simulated solar and artificial light, ACS Appl. Energy Mater. (2025), https://doi.org/10.1021/acsaem.5c01192.
[61] R. Speranza, S. Amenta, P. Zaccagnini, et al., Harnessing γ-Valerolactone: green and low-toxic solvent for enhanced dye-sensitized solar cells performance under indoor lighting, Adv. Energy Sustain. Res. (2025), https://doi.org/10.1002/aesr.202400370.
[62] J. Wu, Z. Lan, J. Lin, et al., Counter electrodes in dye-sensitized solar cells, Chem. Soc. Rev. 46 (2017) 5975–6023, https://doi.org/10.1039/c6cs00752j.
[63] M. Wu, X. Lin, Y. Wang, et al., Economical Pt-free catalysts for counter electrodes of dye-sensitized solar cells, J. Am. Chem. Soc. 134 (2012) 3419–3428, https://doi.org/10.1021/ja209657v.
[64] C. Hora, F. Santos, A.M.V.M. Pereira, et al., PEDOT-graphene counter-electrode for solar and improved artificial light conversion in regular, bifacial and FTO-less cobalt mediated DSSCs, Electrochim. Acta 412 (2022), https://doi.org/10.1016/j.electacta.2022.140140.
[65] Ze Yu, Nick Vlachopoulos, Mikhail Gorlov, et al., Liquid electrolytes for dye-sensitized solar cells, Dalton Trans. 40 (2011) 10278–10288, https://doi.org/10.1039/c1dt11023c.
[66] F. Fabregat-Santiago, J. Bisquert, G. Garcia-Belmonte, et al., Influence of electrolyte in transport and recombination in dye-sensitized solar cells studied by impedance spectroscopy, Sol. Energy Mater. Sol. Cell. 87 (2005) 117–131, https://doi.org/10.1016/j.solmat.2004.07.017. Elsevier.
[67] C.H. Yoon, S.K. Chul, H.H. Ko, et al., Enhanced performance of dye-sensitized solar cells with activated carbons, J. Nanosci. Nanotechnol. 13 (2013) 7875–7879, https://doi.org/10.1166/jnn.2013.8115.
[68] S. Zhang, J. Jin, D. Li, et al., Increased power conversion efficiency of dye-sensitized solar cells with counter electrodes based on carbon materials, RSC Adv. 9 (2019) 22092–22100, https://doi.org/10.1039/c9ra03344k.
[69] N. Kanjana, W. Maiaugree, T. Wechprasit, et al., Preparation of a hierarchical porous activated carbon derived from cantaloupe peel/fly ash/PEDOT:PSS composites as Pt-free counter electrodes of dye-sensitized solar cells, Heliyon 10 (2024) e29957, https://doi.org/10.1016/j.heliyon.2024.e29957.
[70] R. Kumar, V. Sahajwalla, P. Bhargava, Fabrication of a counter electrode for dye-sensitized solar cells (DSSCs) using a carbon material produced with the organic ligand 2-methyl-8-hydroxyquinolinol (Mq), Nanoscale Adv. 1 (2019) 3192–3199, https://doi.org/10.1039/c9na00206e.
[71] A. Mostaccio, F. Bolognesi, V. Appetito, et al., Laser-induced graphitization (LIG) of a mediterranean cultivation softwood: does anisotropy matter? Mater. Res. Bull. 189 (2025) https://doi.org/10.1016/j.materresbull.2025.113460.

[72] X. Liu, D. Lyu, C. Merlet, et al., Structural Disorder Determines Capacitance in Nanoporous Carbons, vol. 384, 2024.
[73] Tutor U. Andrea Lamberti, J. Martínez Rodrigo, Yu Kyoung Ryu, A. Bisceglie, Cellulose Acetate as Novel Precursor to Synthesize Laser Induced Graphene Tutors, 2024.
[74] A. Balducci, W.A. Henderson, M. Mastragostino, et al., Cycling stability of a hybrid activated carbon//poly(3-methylthiophene) supercapacitor with N-butyl-N-methylpyrrolidinium bis(trifluoromethanesulfonyl) imide ionic liquid as electrolyte, Electrochim. Acta 50 (2005) 2233–2237, https://doi.org/10.1016/j.electacta.2004.10.006.
[75] A.C. Lazanas, M.I. Prodromidis, Electrochemical impedance spectroscopy—a tutorial, ACS Measurement Science Au 3 (2023) 162–193, https://doi.org/10.1021/acsmeasuresciau.2c00070.
[76] S. Dsoke, X. Tian, C. Täubert, et al., Strategies to reduce the resistance sources on electrochemical double layer capacitor electrodes, J. Power Sources 238 (2013) 422–429, https://doi.org/10.1016/j.jpowsour.2013.04.031.
[77] R. Ye, Y. Chyan, J. Zhang, et al., Laser-induced graphene formation on wood, Adv. Mater. 29 (2017), https://doi.org/10.1002/adma.201702211.
[78] S.L. Silvestre, T. Pinheiro, A.C. Marques, et al., Cork derived laser-induced graphene for sustainable green electronics, Flexible and Printed Electronics 7 (2022), https://doi.org/10.1088/2058-8585/ac8e7b.
[79] J. Coelho, R.F. Correia, S. Silvestre, et al., Paper-based laser-induced graphene for sustainable and flexible microsupercapacitor applications, Microchim. Acta 190 (2023), https://doi.org/10.1007/s00604-022-05610-0.